Title:

Missing-In-Metastasis / Metastasis Suppressor 1 modulates B cell receptor signaling, B cell metabolic potential and T cell-independent immune responses.

Sarapulov AV*, Petrov P*, Hernandez-Perez S*, Sustar V*, Kuokkanen E*, Vainio M*, Cords L†, Fritzsche M†, ‡, Carrasco Y§ and Mattila PK*

* *Institute of Biomedicine and MediCity Research Laboratories, University of Turku, Tykistökatu 6B, 20520 Turku, Finland*

† *MRC Human Immunology Unit, Weatherall Institute of Molecular Medicine, University of Oxford, Headley Way, OX3 9DS Oxford, UK*

‡ *Kennedy Institute for Rheumatology, Roosevelt Drive, University of Oxford, Oxford OX3 7LF Oxford, UK*

§ *Department of Immunology and Oncology, Centro Nacional de Biotecnología (CNB)-CSIC, Madrid, Spain*

Corresponding author:
Pieta Mattila
Tel: +358 2 333 7935
Fax: +358 2 333 7000
E-mail: pieta.mattila@utu.fi

Keywords: MIM, MTSS1, I-BAR, B cell receptor signaling, BCR, B cell activation, adaptive immune response, metabolism, T-independent immune response

Abstract

Efficient generation of antibodies by B cells is one of the prerequisites of protective immunity. B cells, activated by cognate antigens via B cell receptors (BCR) or pathogen-associated molecules through pattern-recognition receptors, such as TLRs, initiate signaling cascades leading to transcriptional and metabolic changes that ultimately transform B cells into efficient producers of antibodies. BCR signaling is also critical for normal development, as well as survival, of B cells, and critical for survival of different types of lymphomas. A number of steps initiated downstream of BCR rely on coordinated action of actin cytoskeleton, which is in turn dependent on concerted action of multiple actin-regulatory proteins, some of them exclusive to B cells. In our study we dissect the role of Missing-In-Metastasis, or Metastasis suppressor 1 (MIM, or MTSS1), a membrane- and actin cytoskeleton-associated I-BAR domain protein, in the regulation of B cell-mediated immunity. Differential expression of MIM has been associated with variety of cancers, whereas loss of MIM was found to lead to development of B cell lymphomas in adult mice, suggesting important functions in B cells. We take advantage of MIM knockout mouse strain and show normal B cell development and composition of B cell compartments in the periphery. However, we found that MIM-deficient B cells are defected in BCR signaling in response to surface-bound antigen and have higher metabolic activity after activation with LPS or CpG. *In vivo* MIM knockout animals exhibit impaired IgM antibody responses to immunization with T cell-independent antigen. This study provides first comprehensive characterization of MIM in B cells and highlights its modulatory role for B cell-mediated immunity.

Introduction

Appropriate adaptive immune responses, including efficient clearing of pathogens while maintaining the homeostasis of the host, depend on fine-tuned balance of various signals. Increasing evidence points towards an important role of the actin cytoskeleton and plasma membrane organization at the cross-roads of various signaling pathways orchestrating lymphocyte action (Mattila et al., 2016). In B cells, the actin cytoskeleton enables changes in cell morphology, required, for instance, during the formation of the immunological synapse. Interestingly, actin cytoskeleton and plasma membrane also potently regulate B cell receptor (BCR) signaling (Kuokkanen et al., 2015; Mattila et al., 2013, 2016; Treanor et al., 2010). A plethora of cytoskeletal regulator proteins enable the multifaceted roles of actin cytoskeleton in living cells. Lymphocytes generally present very characteristic protein expression patterns and considering the specialized functions of these immune cells, it is not surprising that this also holds true for the regulators of the actin cytoskeleton. One best-known example of such protein is actin nucleator, Wiscott-Aldrich syndrome (WAS) protein (WASp), a critical regulator of lymphocyte function (Bosticardo et al., 2009).

Another protein linked to the regulation of both the actin cytoskeleton and the plasma membrane that shows particularly high expression in lymphocytes (Mattila et al., 2003; and information based on BioGPS portal), is a highly conserved protein Missing in Metastasis (MIM), or Metastasis Suppressor 1 (MTSS1). MIM belongs to a family of proteins with characteristic inverse Bin, Amphiphysin, Rvs (I-BAR; or IRSp53, MIM (IMD)) domain, which binds and deforms cellular membranes (Mattila et al., 2007; Yamagishi et al., 2004). It also directly interacts with and regulates actin via its C-terminal WH2 domain (Wiskott-Aldrich syndrome homology region 2) (Bompard et al., 2005; Gonzalez-Quevedo et al., 2005; Lee et al., 2007; Mattila et al., 2003; Woodings et al., 2003) and indirectly via interaction with actin cytoskeleton regulatory proteins, such as cortactin (Cao et al., 2012; Lin et al., 2005) and Rac1 GTPase (Bompard et al., 2005; Mattila et al., 2007). These activities place MIM at the interface of the plasma membrane and cellular cytoskeleton. Interestingly, MIM has been linked to various cancers, either as a putative tumor metastasis suppressor, or promoting factor (Machesky and Johnston, 2007). Regarding hematopoietic malignancies, MIM is upregulated, for example, in hairy cell and mantle cell lymphomas as well as chronic lymphocytic leukaemia (CLL) (Petrov et al., 2019, Oncomine portal). In CLL, interestingly, the good prognosis samples exhibit highest levels of MIM while the poor prognosis samples show lower MIM levels in comparison (Petrov et al., 2019). Furthermore, it has been reported that upon aging MIM-deficient mice develop lymphomas resembling diffuse large B cell lymphoma (DLBCL) (Yu et al., 2012). In another MIM-deficient mouse line, a degenerative kidney disease, potentially linked to impaired cell-cell junction formation, was found (Saarikangas et al., 2011). These findings illustrate the complexity of MIM function,

the basis of which remains enigmatic due to the lack of understanding about the molecular mechanisms and pathways where MIM acts.

In this study, we took advantage of a MIM-deficient mouse model (Saarikangas et al., 2011) to explore, for the first time, the physiological role of MIM in B cell compartment, specifically in early B cell activation and mounting of the immune responses. While we found no defects in B cell development, MIM-deficiency caused a variety of changes in mature B cells. MIM$^{-/-}$ B cells showed significantly reduced signaling upon stimulation with surface-bound antigens that mimics activation via immunological synapse. T cell-independent IgM responses were also reduced in MIM-deficient mice. However, T cell-dependent immune responses were normal, likely compensated by other signals and the tendency for higher metabolic activity that we found in MIM-deficient B cells in response to TLR activation with.

Results

Largely normal B cell development and maturation of B cells in MIM-deficient mice

Mice with targeted disruption of *Mtss1* gene, lacking the expression of MIM, were generated previously (Saarikangas et al., 2011). Splenic B cells, that normally show robust MIM staining in immunoblot, isolated from these mice showed no detectable MIM expression in the tissues examined (Suppl. Fig. 1). To investigate the possible roles of MIM in the functions of B cell compartment, we first went on to examine the development of B cells in the bone marrow. We found no apparent differences in the numbers of CD19^{+} and CD19^{+} IgM^{+} populations between age-matched wild type (WT) and MIM$^{-/-}$ mice (Fig. 1A). We then carried out more detailed analysis of the bone marrow B cells with additional surface markers to resolve consecutive developmental stages from common lymphoid progenitors to immature B cells (gating strategy: Suppl. Fig. 1-1). We found no significant differences throughout B cell developmental stages between WT and MIM$^{-/-}$ mice (Fig. 1B). This finding was somewhat surprising taken into account the abberant frequencies of CD19^{+} cells in the spleen and bone marrow of another MIM$^{-/-}$ mouse strain reported by Zhan and colleagues (Yu et al., 2012). We verified our finding by analyzing pre-B cells with gating strategy identical to the one employed by Yu and colleagues, but were not able to detect abnormalities (Suppl. Fig. 1-2).

Next we went on to analyze the maturation of B cells and their different subsets in the periphery. No defects were observed in the overall percentages of CD19^{+} B cells or major T cell subsets in the spleen (Fig. 1C). Similarly, the proportions of transitional (T1–3) and follicular (Fo) B cells were not significantly altered and only mild tendency was observed for elevated MZ B cell compartment. (Fig. 1D). To analyze composition of peritoneal B cells, we isolated cells from the peritoneal cavity of

MIM$^{-/-}$ and WT mice. Again, we found no significant differences in the proportions of CD5^{+} (B1a), CD5^{-} (B1b) or mature peritoneal B cells (B2) (Fig. 1E). These results demonstrate that normal development of different B cell subsets, both in the bone marrow, as well as in the periphery, do not depend on MIM. On the other hand, these findings also highlight possible variation between the two different published MIM-deficient mouse models (Saarikangas et al., 2011; Yu et al., 2012).

MIM-deficient B cells are defected in BCR signaling upon activation with surface-bound antigens

While previous cell biological studies in other cell types, supported by various biochemical assays, have proposed a role for MIM at the interface of the plasma membrane / actin cytoskeleton interface, which regulates receptor function in B cells, we went to examine the role of MIM in BCR signaling. First, we analyzed the mobilization of intracellular calcium in mature B cell populations of spleen and peritoneal cavity upon surrogate antigen stimulation. Splenic B cells were loaded with Fluo-4 and Fura-Red, stimulated with anti-IgM antibodies and analyzed by flow cytometry. Ratiometric analysis of Fluo-4/Fura-Red fluorescence intensities revealed similar elevation of intracellular Ca^{2+} levels in both WT and MIM$^{-/-}$ B cells (Fig. 2A). Peritoneal cavity B cells were loaded with Fluo-4, prestained with CD23-Ax594 just before acquisition and stimulated with anti-IgM-Ax633 antibodies, which allowed distinction between B1 (IgM^{+} CD23^{-}) and B2 (IgM^{+} CD23^{+}) cells. Intracellular Ca^{2+} mobilization was comparable between WT and MIM$^{-/-}$ peritoneal cavity B cells in these two B cell subsets (Suppl. Fig. 2).

Next, we analyzed activation of individual components of BCR signaling pathway by looking at phosphorylation levels of downstream effector molecules. Splenic B cells were stimulated with soluble or surface-bound anti-IgM antibodies for 3, 7 and 15 min and analyzed by immunoblotting. As expected, both stimulatory conditions induced rapid activation of BCR signaling components, as seen from their respective phosphorylation levels. MIM$^{-/-}$ B cells showed clear defects in signaling in response to surface-bound anti-IgM. Activation of most of the analyzed molecules, including Syk, CD19, Btk, p65 NF-κB and MAPK1/2 was significantly reduced (Fig. 2C). In addition, phospho-PI3K showed a trend of reduction, however, not statistical significance. The extent to which early BCR signaling defect was influencing downstream cascades appeared to alternate. The defects in PI3K pathway were largely salvaged at the level of Akt. At the same time, the levels of pp65 NF-kB and pMAPK1/2 were decreased, suggesting that MIM$^{-/-}$ B cells were inefficient in triggering the diacylglycerol (DAG)-PKC module, targets of which both NF-kB and MAPK1/2 are (Mérida et al., 2010). Interestingly, when we studied activation of BCR by soluble ligand, anti-IgM surrogate antibodies in solution, MIM$^{-/-}$ B cells only showed significant defects in the activation of the proximal kinase Syk, but normal activation of other signaling components (Suppl. Fig. 2). These results place MIM as a regulator of, specifically, BCR

signaling by surface-bound antigen, function that clearly depends on the fine-tuned activities of the actin cytoskeleton (Bolger-Munro et al., 2019) and could fit well with the previously postulated role of MIM as an organizer of the actin cytoskeleton-membrane interface.

The morphology and formation of the immunological synapse is unaltered in MIM-deficient B cells

To see if MIM-deficient B cells showed any changes in the overall morphology, we visualized them using scanning electron microscopy (SEM), either in steady-state or after 10 min activation by surface-tethered anti-IgM, mimicking formation of the immunological synapse. The morphology of MIM$^{-/-}$ B cells appeared similar to WT cells (Fig 3A). Next, inspired by the diminished activation of BCR signaling pathways upon surface-bound antigen stimulation in MIM$^{-/-}$ cells, we activated B cells on anti-IgM-coated coverslips and analyzed the area of spreading using TIRF microscopy. TIRF microscopy is a method that allows visualization of the membrane-cover slip interface with approximately 150 nm depth providing better signal to noise in this region without disturbance by the signals from deeper parts of the cell. We noted that MIM$^{-/-}$ B cells had a tendency to spread less than their WT counterparts (Fig. 3B). To measure overall phosphorylation at the contact region we stained the cells with anti-phospho-Tyrosine (pTyr) antibodies. Mean fluorescence intensities of pTyr staining were also reduced in MIM$^{-/-}$ B cells, however, the difference to WT appeared smaller as compared to the difference observed in immunoblotting (Fig. 2B, C). These results indicate that lower amount of engaged antigen due to inefficient spreading response may contribute to the ultimate signaling defect observed in MIM$^{-/}$- B cells upon activation with surface-bound anti-IgM antibodies. At the same time, based on the F-actin staining on these cells, we concluded that despite of diminished area of spreading, MIM$^{-/-}$ cells did not exhibit major morphological differences in their actin cytoskeleton (Fig. 3B).

Recognition of surface-bound antigens *in vivo* can involve both stiff substrates and various mobility ligands. While stiff substrates can include bacterial cell wall components or extracellular matrix-linked antigens, perhaps most typical encounter occurs on the surface of antigen presenting cells, where antigens remain laterally mobile. To understand if MIM$^{-/-}$ B cells can initiate robust BCR signaling upon encounter with mobile antigens, we first settled Fluo-4-loaded WT and MIM$^{-/-}$ B cells on supported lipid bilayers (SLB), containing Ax647-labeled anti-kappa antibodies and ICAM-1. Mobilization of Ca^{2+} was imaged for 5 min by confocal microscopy and analyzed with CalQuo^2 software (Lee et al., 2017). Analysis of median Fluo-4 intensity and proportions of MIM$^{-/-}$ B cells with single peak or oscillatory Ca^{2+} intensity profiles revealed no differences between MIM$^{-/-}$ and WT cells (Fig. 3C). Furthermore, during contraction phase of the IS formation, MIM$^{-/-}$ B cells accumulated similar amounts of anti-kappa

surrogate antigen in the center of the IS as WT B cells, displaying normal IS organization at 10 min timepoint (Fig. 3D). These results suggest that while MIM modulates BCR signaling and spreading responses upon antigen contact on stiff substrates, it appears largely dispensable for overall immunological synapse formation upon engagement of membrane-bound mobile antigens.

MIM is required for efficient antibody responses against T-independent antigen

To test if the defected signaling in MIM-deficient B cells leads into problems in mounting of the immune responses, we went on to examine antibody levels of our mice first at the basal state and then upon immunization with T cell-independent or T cell-dependent model antigens. We saw no significant changes in the basal antibody levels in the sera of WT and MIM$^{-/-}$ mice, although especially IgG1 appeared slightly diminished (Fig. 4A). To study development of antibody responses towards T-independent antigens, we immunized mice with NP-FICOLL (Fig. 4B). Notably, we found a clear reduction in the levels of both total and NP-specific IgM in MIM-deficient mice (Fig. 4B). Interestingly, we also detected impaired responses in the total levels of IgG subtypes, most profound in IgG2b, while generation of NP-specific IgG responses was normal.

For immunizations with T-dependent protein antigen, we used NP-KLH in Alum and followed up the primary response for four weeks. Four months later, we stimulated a memory response and followed that for 2 weeks (Suppl. Fig. 4A). Somewhat surprisingly, we found that MIM$^{-/-}$ mice were as efficient in mounting antibody responses to a protein antigen as their WT counterparts (Suppl. Fig. 4B). Analysis of the memory responses also showed equal levels of NP-specific IgG for all subclasses (Suppl. Fig. 4C). Furthermore, we analyzed affinity maturation by comparing binding to low and high densities of NP-epitopes in ELISA, and found also no significant differences between WT and MIM-/- mice (Suppl. Fig. 4D).

In the light of defects in BCR signaling and T-independent immune responses in MIM-deficient mice, normal antigen-specific IgG immune responses may point towards compensation by other signals in the system, such as T cells help. To dissect the B cell intrinsic features linked to IgG antibody responses in more detail, we set up an *in vitro* assay for class-switch recombination (CSR). Here, we provoke B cells to change the isotype of the produced Ig molecules, by mimicking cellular events of pathogen encounter or T cell help during maturation of IgG antibody responses. As expected, activation of B cells with LPS or CD40L in combination with cytokines for 3 days induced switching of surface-expressed Ig molecules to different IgG isotypes, as detected by flow cytometry. Consistent with the *in vivo* data on generation of NP-specific IgG antibody responses, MIM$^{-/-}$ B cells switched normally in all

tested conditions, producing similar percentages of IgG^+ cells, indicating that MIM is not required for CSR in response to TLR ligands or CD40L and cytokines (Suppl. Fig 5A, B, C). In fact, switching rates were even slightly higher for MIM KO B cells in LPS cultures (Suppl. Fig. 5A, C). We also loaded the cells with Cell Trace Violet dye, which allowed us to analyze fluorescence profiles of dividing splenic B cells in response to these stimuli. We found robust proliferation of $MIM^{-/-}$ B cells when they were activated with LPS, CD40L or anti-IgM + CD40L (Suppl. Fig. 5D). Analysis of the proliferation indices (PI) showed equal proliferation of $MIM^{-/-}$ and WT cells, however, the division indices (DI) of $MIM^{-/-}$ B cells were moderately increased in CD40L + IFNγ cultures, reflecting smaller numbers of undivided cells detected in cultures on day 3.

Taken together, our immunization studies suggest that MIM plays a role in IgM antibody responses to T cell-independent antigens, however, is dispensable for the development of antibodies against T cell-dependent protein antigens.

$MIM^{-/-}$ B cells show higher metabolic profile upon LPS and CpG stimulation

Immunity-related signaling pathways are tied to general cell metabolism, which not only responsible for energy production but also has an impact on signal propagation and transcription through abundance of energy sources and actions of key metabolic enzymes and metabolites (Jellusova, 2018; O'Neill et al., 2016). We used Seahorse platform to analyze metabolic reprogramming of B cells upon activation of BCR or TLRs. To this end, splenic B cells from WT and $MIM^{-/-}$ mice were cultured for 24 h with either anti-IgM with IL-4, or TLR agonists LPS or CpG. The rates of cellular oxygen consumption (OCR), an estimate of mitochondrial respiration, and extracellular acidification (ECAR), an estimate of glycolysis, were measured with a Seahorse Mito Stress test. In this assay, serial injections of oligomycin, FCCP and antimycin A / rotenone mixture, sequentially inhibit ATP production, collapse the proton gradient membrane potential and finally shut down mitochondrial respiration. This system allows measurement of the basal OCR, maximal and spare respiratory capacities, as well as determination of non-mitochondrial respiration.

In general, B cell activation is expected to result in increase in both, OCR and ECAR as the cells shift from resting state into activated phenotype (Akkaya et al., 2018; Caro-Maldonado et al., 2014; Price et al., 2018). We activated WT and $MIM^{-/-}$ B cells with LPS, CpG and IgM + IL-4 for 24 h or kept them largely resting with IL-4 alone. Notably, we saw a significant increase in the metabolic profile of MIM-/- cells as compared to WT counterparts upon activation with TLR ligands, LPS or CpG (Fig. 5A, B). We observed approximately 30% increase in the basal metabolic activity as well as maximal respiratory capacity. The spare respiratory capacity showed over two-fold increase in $MIM^{-/-}$ cells upon LPS activation, while with CpG activation, we found variability too high to conclude on the possible

difference. In contrast to TLR stimulations, BCR activation with soluble anti-IgM showed no difference between WT and MIM$^{-/-}$ cells, neither at the basal or maximum respiration levels. Similarly, the levels of glycolytic metabolism, reflected by ECAR values obtained from the same assay, showed elevated levels of glycolytic metabolism in MIM$^{-/-}$ B cells when stimulated with TLR ligands but not IgM + IL-4 (Suppl. Fig. 6). While B cells cultured with IL-4 alone, IgM + IL-4 or LPS showed no change in the predominant route of generated ATP, we observed that basal metabolic activity was shifted to oxidative metabolism in MIM$^{-/-}$ B cells stimulated with CpG (Fig. 5C).

Next we asked if the higher metabolic activity of MIM$^{-/-}$ B cells reflects a bona fide change in the mitochondrial activity or is a result of elevated mitochondrial biogenesis upon TLR-mediated metabolic reprograming. To this end, we stained B cell mitochondria with antibodies against TMRE and Tom20 to assess mitochondrial membrane potential and mitochondrial mass, respectively. Already in freshly isolated splenic MIM$^{-/-}$ B cells, we found normal levels of mitochondrial potential, however, slightly elevated mitochondrial mass without noticeable increase in mitochondrial membrane potential (Fig. 5D). However, TLR-activated B cells from WT and MIM$^{-/-}$ B cells had comparable levels of both mitochondrial membrane potential and mitochondrial content, suggesting that higher metabolic activity in TLR-stimulated MIM$^{-/-}$ B cells was not a result of increased mitochondrial biogenesis, but reflected increased mitochondrial activity (Fig. 5E).

Thus, we showed that MIM$^{-/-}$ B cells have higher metabolic activity after short-term culture with LPS or CpG TLR ligands and, although these differences do not persist after 3d cultures (data not shown), we believe that such metabolic change may influence, for instance, kinetics of antibody responses to TI-1 antigens.

DISCUSSION

Predisposition of another MIM-deficient mouse strain to lymphomagenesis, reported by Zhan and colleagues, is intriguing (Yu et al., 2012). We have not performed aging experiments to follow lymphomagenesis in our MIM$^{-/-}$ strain, however, BCR signaling is one of the main survival pathways in different types of lymphoma and dysregulated wiring of BCR signaling could play a role in lymphomagenesis (Young and Staudt, 2013). Unlike originally reported by Zhan and colleagues (2012), B cell development appeared normal in our MIM$^{-/-}$ strain also when gating strategy identical to Zhan and colleagues was applied (Suppl. Fig. 1-2). Confusingly, in the first studies with their MIM-deficient strain, Zhan and colleagues reported abberant levels of total CD19^{+} or CD19^{+}IgM^{+} cells in the lymphoid

organs (Yu et al., 2012). However, in the later studies, the same group failed to find the phenotype anymore (Zhan et al., 2016). The observed discrepancies may, thus, potentially arise from the differences in strain maintenance or, for instance, from different age of mice at the time of immunophenotyping. The mouse strain generated by Zhan and colleagues used embryonic stem cells (ES; clone CSC156, BayGenomics) with insertion of gene trap sequence between exons 3 and 4 (Yu et al., 2011). Notably, an independent attempt to recapitulate the generation of MIM knock out strain with the same clone of ES cells (CSC156, BayGenomics) resulted in inefficient use of delivered splicing acceptor (SA) site and considerable expression of full-length Mtss1 mRNA as well as protein expression (Fahrenkamp et al., 2017). This data warrants careful interpretation of the studies made with mouse model based on CSC156 gene trap ES cells. However, we cannot rule out the possibility that different genetic background of the mouse strains used for backcrossing in these studies (C57Bl/6 vs FVB/N) may influence activity of the spliceosome. Furthermore, variation in the remaining expression levels between the animals seems notable, indicating lability of the splicing. Lack of protein MIM expression in analyzed cells was, however, shown by Zhan and colleagues (Yu et al., 2011, 2012). In our strain, based on the insertion of neomycin cassette with several stop codons in the first exon of *Mtss1* sequence, low levels of alternative splicing generating a transcript has been previously observed. However this transcript translates into a N-terminally truncated protein that has functionally inhibited critical I-BAR domain, and which also did not lead to detectable protein expression in MIM$^{-/-}$ animals (Saarikangas et al., 2011). We confirmed clear and repeatable lack of detectable protein expression in our substrain using two different commercial antibodies (Suppl. Fig. 1-1).

In this study, by observing consistently diminished phosphorylation of several BCR effector molecules, we show that MIM$^{-/-}$ B cells are defected in their ability to signal upon stimulation of BCR with surface-bound antigens (Fig. 2B). Signaling upon soluble antigen stimulation, on the other hand, was mostly normal showing only slight diminution in the levels of pSyk (Suppl. Fig. 2). Although, diminished spreading may contribute to the signaling defect seen in response to surface-bound antigen, the area of spreading was not drastically lower (Fig. 3B). This suggests that MIM participates in the ability of B cells to discriminate different types of antigens by playing a specific role in B cell activation on surfaces. Although the differential responses of B cells to different forms of antigen are nowadays widely accepted (Snapper, 2018), to our knowledge there are only few molecules, such as CD19 (Depoil et al., 2008), that have been reported to specifically regulate stimulation by surface-linked antigens with mechanisms likely separate from structural roles in cell adhesion or spreading.

Our experiments on supported lipid bilayers (SLB) showed, however, that MIM$^{-/-}$ B cells are able to form signaling-competent BCR-Ag microclusters and gather normal amounts of antigen in the center of

the IS (Fig. 3D). This suggests that coupling of BCR to actin and microtubule cytoskeleton, required for the cell spreading and antigen gathering, respectively (Liu et al., 2012; Schnyder et al., 2011), is not notably defected in these settings. However, results from SLB, which are laterally fluid, cannot be directly compared with B cell stimulation on immobilized surrogate antigens or a situation where B cell need to overcome frictional coupling of antigen-presenting molecules to the membrane skeleton of the APC. In addition, SLBs in our experiments were functionalized with ICAM-1, which is known to lower the threshold for B cell activation (Carrasco et al., 2004).

We found that stimulation with surface-bound antigen results to a certain degree in reduced phosphorylation of all the tested BCR effectors in MIM$^{-/-}$ B cells, but also noted that defects in early BCR signaling, exemplified by reduced pSyk and pCD19, did not propagate evenly downstream. Reduced pCD19 seemed to largely spare PI3K pathway as pAkt levels are on par with those of WT (Otero et al., 2001) (Fig. 2B, C). At the same time, levels of both pNF-kB and pMAPK1/2 at later time points (7 and 15 min) are significantly reduced, suggesting that defect lies at the level of DAG-PKC signaling module (Coughlin et al., 2005; Mérida et al., 2010; Su et al., 2002). This is interesting in the light of study pointing on the role of PKC-FAK axis in the regulation of force-dependent B cell activation (Shaheen et al., 2017), which we think is consistent with our results of specific defects in response to surface-bound antigens.

We found that MIM-deficient mice developed impaired IgM antibody responses to NP-FICOLL immunizations. On the other hand, the responses appeared normal in NP-KLH immunization, indicating that the defect in the antibody production is specific to the nature of the antigen. FICOLL polysaccharide haptenated with NP, or other small molecule epitope, is a typical T cell-independent type 2 (TI-2) antigen and, in contrast to TI-1 antigens, is unable to induce humoral immune responses in *Btk*-deficient CBA/N strain and normal neonatal mice reflecting dependence on mature B cell populations (Scher, 1982). Marginal zone B cells and peritoneal cavity B1b cells are, together, thought to be responsible for hapten-specific antibody production upon immunization with FICOLL conjugates (Girkontaite et al.; Guinamard et al., 2000; Haas, 2011). We show that MIM$^{-/-}$ mice have comparable proportions of B1b, B1a and B2 cells in the peritoneal cavity (Fig. 1F) and normal composition of splenic B cell compartments, perhaps with slight tendency to have elevated MZ B cell numbers (Fig. 1D), suggesting that disproportions in mature B cells populations of spleen and peritoneal cavity are unlikely to cause the reduced anti-NP IgM levels (Fig, 4B). As the numbers of CD4^{+} T cells (Fig. 1C) and antibody responses to T cell-dependent antigen NP-KLH (Suppl. Fig. 4), as well as the levels of class-switched IgG antibodies to NP-FICOLL itself, appeared normal (Fig. 4B), we also consider the defects in possible

indirect T cell help very unlikely. Therefore, we suggest that the defected NP-FICOLL responses in MIM$^{-/-}$ mice are likely to be caused by defected B cell receptor-mediated signaling. Indeed, we observe that MIM-deficient splenic B cells exhibit diminished BCR signaling on anti-IgM-coated surfaces (Fig. 2B, C). Thus, our results would be in line with the observations that *in vivo* B cells recognize and respond to antigens that are immobilized on the surface of other cells in the secondary lymphoid organs (Carrasco and Batista, 2007). FICOLL is a long chain polysaccharide with high molecular weight of ~400 kDa, which is unable to enter conduit system of the spleen for direct access to follicular areas (Nolte et al., 2003). However, both, i.v. and i.p. delivery of FICOLL conjugates results in its accumulation in the marginal zone and later in the follicular regions of the spleen (Cinamon et al., 2008; García de Vinuesa et al., 1999). Such follicular localization of TD and TI antigens has been described as a result of complement-dependent antigen capturing by non-cognate MZ B cells and delivery to follicular areas for deposition onto follicular dendritic cells (FDC) for continuous display to antigen-specific B cells (van den Eertwegh et al., 1992; Ferguson et al., 2004; Heesters et al., 2013; El Shikh et al., 2010). As it was shown by other studies, antigen presenting surface as well as substrate stiffness prominently influences BCR signaling strength (Wan et al., 2013; Zeng et al., 2015) and, in this respect, FDCs have been reported to serve as rather stiff antigen presenting substrate (Spillane and Tolar, 2017). Thus, we suggest that MIM$^{-/-}$ B cells are defected in being triggered by FDC-displayed NP-FICOLL molecules, similar to BCR stimulation on anti-IgM-coated surface, which results in poor plasmablast differentiation and reduced IgM antibody response.

We also noticed decreasing total IgG levels in the course of the NP-FICOLL response (Fig. 4B). The cause of it is unclear but may include, for instance, inhibition of constitutive antigen presentation in B cells by high load of NP-FICOLL, which MIM$^{-/-}$ B cells are unable to cope with efficiently (González-Fernández et al., 1997). Our data show relatively equal fold-increase of NP-specific IgG of all isotypes in response to NP-FICOLL immunization (Fig. 4B). This is interesting as some TI-2 antigens, including TNP-FICOLL, are reported to elicit IgG3-restricted class switching (Mongini et al., 1981, 1984; Perlmutter et al., 1978; Slack et al., 1980) (García de Vinuesa et al., 1999). However, mouse strain or experimental differences may exist and this might not be generally applied to all TI-2 antigens, for which however, only the levels of IgM and IgG3 are typically tested.

While naive B cells have low metabolic profile, upon activation, they elevate their metabolic rates typically manifested by an increase in oxygen consumption and glycolysis (Caro-Maldonado et al., 2014; Jellusova, 2018). The mitogenic stimuli IgM, LPS and CpG have been shown to dramatically increase metabolic requirements in B cells and thus, play a key role in this transition, essential for the

immune responses and differentiation into antibody secreting cells (Boothby and Rickert, 2017; Jellusova, 2018). Interestingly, we found that after 24h culture with either LPS or CpG, respective stimulators for TLR4 and TLR9, MIM$^{-/-}$ B cells exhibited approximately 30% increased metabolic activity as measured by basal oxygen consumption rate as well as by maximum and spare respiratory capacities (Fig. 5A, B). This finding indicates increased metabolic demands in cells lacking MIM. Further supporting the higher cellular energetics of MIM$^{-/-}$ cells, already at resting state, MIM-deficient B cells had slightly more mitochondrial mass, as detected by Tom20 levels. At the same time, LPS and CpG induced similar levels of increase in mitochondrial mass and membrane potential in both WT and MIM$^{-/-}$ cells (Fig. 5D, E), indicating that metabolic differences do not simply arise from enhanced mitochondrial biogenesis. We also did not observe differences in metabolism when B cells were stimulated with anti-IgM + IL-4, suggesting specificity in the role of MIM towards TLR signaling-induced metabolic changes. The higher energetics in the absence of MIM might indicate that its involvement in TLR4/9 signaling might negatively affect metabolism. Such increased metabolic capacity could also compensate the effects of compromised BCR signaling upon in vivo B cell differentiation and antibody responses to TI-1 antigens. The exact mechanism of such involvement and its role for cellular activation remains to be further investigated, but it is tempting to speculate of a possible link between altered cellular metabolism and the loss of MIM in several cancers.

Materials and Methods

Antibodies and chemicals

Full list of antibodies and reagents used in the study can be found in *supplementary file N.*

Mice, immunizations and serum collection

MIM knockout mouse colony in Turku was established by breedings of HEZ founder mice and had no apparent health problems until the age of 8 months when mice were sacrificed due to possible damaging effects of reported lymphomas later in life (Yu et al., 2012, Mattila unpublished). However, we observed that among 18 genotyped pups that developed hydrocephaly over the study period, 17 were knockout and 1 was heterozygote. None of the mice that developed hydrocephaly were genotyped as wild-type.

Mice with homozygous insertion of Neomycin (*Neo*) gene cassette into exon 1 of *MIM* gene were generated previously (Saarikangas et al., 2011). Briefly, *Neo*-cassette, containing several stop codons, was introduced by homologous recombination into 129/Sv ES-cells. Chimeric mice were backcrossed to C57Bl/6J background for several generations and mice colony in Turku was established by breedings of HEZ founder animals. All experiments were done with age- and sex-matched animals and WT littermate controls were used whenever possible. At the age of 3-4 months, groups of WT and $MIM^{-/-}$ females were immunized with NP_{40}-FICOLL (T-independent, "FICOLL" group) or NP_{31}-KLH (T-dependent, "KLH" group) antigens. Each mouse received 50 µg of antigen in 150 µL of PBS (NP_{40}-FICOLL) or PBS/Alum adjuvant (2:1 ratio) solution by intraperitoneal injection. Blood (~100 µL) was sampled from lateral saphenous veins on day -1 (preimmunization) and every week after immunization on days +7, +14, +21 and +28 for both "FICOLL" and "KLH" group. Secondary (boost) immunization of "KLH" group was performed on day +135 (0) and blood was sampled on days +134 (-1), +139 (+4), +143 (+8) and +150 (+15). Coagulated blood was spun at +4°C / 2000 rpm for 10 min and serum was collected and stored at -20°C.

All animal experiments were approved by the Ethical Committee for Animal Experimentation in Finland. They were done in adherence with the rules and regulations of the Finnish Act on Animal Experimentation (62/2006) and were performed according to the 3R-principle (animal license numbers: 7574/04.10.07/2014, KEK/2014-1407-Mattila, 10727/2018).

ELISA

Total and NP-specific antibody levels were measured by ELISA on half-area 96-well plates. Capture antibodies (2 µg/mL) or NP-conjugated carrier proteins ($NP_{(1-9)}$-BSA or $NP_{(>20)}$-BSA at 50 µg/mL) were coated at +4°C overnight in 25 µL of PBS. Non-specific binding sites were blocked for 2 hours in 150

μL of blocking buffer (PBS, 1%BSA, 0.05 NaN_3). Appropriate dilutions of 50 μL serum samples in blocking buffer were added for overnight incubation at +4°C. Biotin-conjugated detection antibodies (2 μg/mL) in 50 μL of blocking buffer are added for 1 hour followed by 50 μL AP (alkaline phosphatase)-streptavidin (1:5000) in blocking buffer for 1 hour at room temperature (RT). In between all incubation steps, plates were washed with 150 μL washing buffer (PBS, 0.05% Tween-20) 3 times (steps before sample addition) and 6 times (after). The final wash was completed with 2 times wash with 150 μL of mQ water. Finally, 50 μL of AP-substrate solution was added and and OD was measured at 405 nm. Appropriate serum dilutions were determined experimentally to fall into linear part of the dose-response curve of the absorbance measurements for any given isotype and typical values are as follows: IgM levels (1:3000–1:4000), IgG levels (1:20000–1:80000). Different dilutions of AP-streptavidin were used where necessary. Typical time for AP-substrate incubation before measurement was about 30 min at RT.

All ELISA samples were run in duplicates, OD values were averaged and blank background was subtracted. Absolute concentrations of total antibody levels were extrapolated from calibration curves prepared by serial dilution of mouse IgM or subclasses of IgG from C57Bl/6 immunoglobulin panel. Relative NP-specific antibody levels were extrapolated from reference curves prepared by serial dilution of pooled serum, in which the highest dilution step received an arbitrary unit of 0.5.

Immunophenotyping

All cells were isolated using B cell isolation buffer (PBS, 2% FCS, 1mM EDTA). Bone marrow cells were isolated by flushing the buffer through mouse femoral and tibial bones. Splenocytes were isolated by mashing the spleen in small buffer volumes with syringe plunger in 48-well plates. Peritoneal cavity cells were isolated by filling the cavity with ~ 10 mL buffer volume through puncture and collecting the fluid back. Cell suspensions were filtered through 70 μm nylon cell strainers, and as a general flow cytometry protocol all following steps were done in flow cytometry buffer I (PBS, 1% BSA). Fc-block was done with 0.5 μL/70 μL anti-mouse CD16/32 antibodies for 10 min and cells were stained for 30 min. Washings were done 3 times in 150 μL of flow cytometry buffer I. All steps were carried out on ice in U-bottom 96-well plates at cell density of 0.25–0.5 × 10^6/well. Before acquisition cells were resuspended in 130 μL flow cytometry buffer II (PBS, 2.5% FCS). Samples were acquired on BD LSR Fortessa, equipped with four laser lines (405 nm, 488 nm, 561 nm, 640 nm) and data was compensated and analyzed with FlowJo software.

B cell isolation

Splenic B cells were Isolated with EasySep™ Mouse B Cell Isolation Kit (Stem Cells Technologies) according to manufacturer's instructions and let to recover in complete RPMI (10% FCS, 20 mM HEPES, 50 µM β-mercaptoethanol, 1:200 Pen/Strep 10K/10K) (+37°C, 5% CO_2) for 1-2 hours.

Class-switch recombination, proliferation

Isolated splenic B cells (~10–20 × 10^6 cells) were stained first with 5 ul (5mM) Cell Trace Violet in 10 mL of PBS for 10 min, RT and let to recover in complete RPMI (+37°C, 5% CO_2) for 1–2 hours. To induce class-switching, B cells were cultured on 24-well plates at 0.5 × 10^6/mL density in complete RPMI supplemented with indicated doses of LPS (4 µg/mL), CD40L (150 ng/mL), IL-4 (5 ng/mL), IFN-γ (100 ng/mL) and TGF-β (3 ng/mL) for 3 days. Cells were blocked with anti-mouse anti-CD16/32 and stained for 30 min with antibodies against IgG subclasses. Additionally, cells were stained with 7-AAD (4 µg/mL) for live/dead cell discrimination and samples were acquired on BD LSR II equipped with 3 laser lines (405 nm, 488 nm, 640 nm) and analyzed with FlowJo software.

B cell receptor signaling and immunoblotting

For analysis of BCR signaling, isolated splenic B cells were starved for 10 min in plain RPMI and 0.5 × 10^6 cells were stimulated in duplicates with either soluble (5 µg/mL) in 96-well plates or surface-bound anti-mouse IgM, µ-chain-specific antibodies (48-well plates) in 100 µL of plain RPMI for 3, 7 and 15 min. For surface-bound mode, plates were coated with 5 µg/mL of anti-IgM antibodies in 120 µL of PBS at +4°C, overnight and washed 3 times with 500 µL of ice-cold PBS before experiment. B cells were instantly lysed with 25 µL of 5x SDS lysis buffer (final: 62.5 mM TrisHCl pH ~6.8, 2% SDS, 10% Glycerol, 100mM β-mercaptoethanol, bromphenol blue) and sonicated for 7.5 min (1.5 mL tubes, high power, 30 s on/off cycle, Bioruptor plus, Diagenode). Lysates (20–30 µL) were run on 8–10% polyacrylamide gels and transferred to PVDF membranes (Trans-Blot Turbo Transfer System, Bio-Rad). Membranes were blocked with 5% BSA in TBS (TBS, pH ~7.4) for 1 hour and incubated with primary antibodies (~1:1000) in 5% BSA in TBST (TBS, 0.05% Tween-20) at +4°C, overnight. Secondary antibody incubations (1:20000) were done for 2 hours at RT in 5% milk in TBST for HRP- and with addition of 0.01% SDS for far-red-conjugated antibodies. Washing steps were done in 10 mL of TBST for 5 × 5 min. Membranes were scanned with Odyssey CLx (LI-COR) or visualized with Immobilon Western Chemiluminescent HRP Substrate and ChemiDoc MP Imaging System (Bio-Rad). Phospho-antibodies were stripped in 25mM Glycine-HCl buffer, pH ~2.5 for 10 min, membranes were blocked and probed again for evaluation of total protein levels. Images were background subtracted and raw integrated densities for each band were measured in ImageJ. Ratios of phosphorylated-vs-total protein

levels were analyzed with ratio paired t test. For data presentation these ratios were normalized to WT value at 0 min.

Intracellular Ca^{2+} flux

Splenic B cells were resuspended at a concentration of 2.5×10^6 cell/mL in RPMI (20 mM HEPES, 2.5% FCS) and loaded with 1 μM Fluo-4 and 5 μM Fura Red for 45 min (+37°C, 5% CO_2). Cell suspension was then diluted in 10 volumes of complete RPMI and incubated for 10 min at RT. Cells were centrifuged at 200 g, at RT for 5 min and resuspended at 2.5×10^6 cells/mL in PBS (20 mM HEPES, 5 mM glucose, 0.025% BSA, 1 mM $CaCl_2$, 0.25 mM sulfinpyrazone, 2.5% FCS). Anti-mouse IgM antibodies were added into prewarmed (+37°C) B cell suspension aliquots to a final concentrations of 5 or 10 μg/mL and cells were acquired on BD LSR Fortessa. Fluorescence of Fluo4 and FuraRed was recorded by a continuous flow for 5 min. Data was analyzed in FlowJo and presented as ratiometric measurement of Fluo4/FuraRed median intensity levels.

Peritoneal cavity B cells were washed in L-15 medium, resuspended in 75 μL acquisition buffer (HBS:L-15 (1:1 ratio), 2.5 μM probenecid) and labeled by addition of 75 μL acquisition buffer with 10 μM Fluo4 for 5 min at +37°C. Cells were washed in 1 ml, resuspended in 200 μL and divided into two wells. B cells were prestained for 10 min on ice with anti-CD23-Ax594 antibodies, washed and resuspended in 100 μL of acquisition buffer on ice. B cell aliquots were prewarmed (+37°C) in a total volume of 300 μL of acquisition buffer and 50 μL of anti-IgM $F(ab)_2$-Ax633 were added. Cells were acquired on BD LSR Fortessa for 3-5 min and analyzed in FlowJo.

Microscopy / Cell spreading

MatTek dishes wells were coated with 5 μg/mL and 7.5 μg/mL anti-mouse IgM, μ-chain-specific antibodies in PBS at +37°C for 30 min and washed once with PBS. Isolated splenic B cells (10^6) were left unstained or labeled with 0.17 μL of anti-B220-Alexa-647 antibodies in 400 μL PBS for 10 min in 1.5 mL tubes on ice, spun (2500 rpm, 5 min), washed twice in 900 μL of ice-cold PBS and resuspended in 200 μL of Imaging buffer (PBS, 10% FBS, 5.5 mM D-glucose, 0.5 mM $CaCl_2$, 0.2 mM $MgCl_2$). Equal amounts of unstained and labeled cells of different genotypes were mixed and loaded onto coated MatTek dishes at 35 μL/well. Cells were incubated for 10 min (+37°C, 5% CO_2), fixed in pre-warmed (+37°C) 4% formaldehyde/PBS for 10 min (RT), permeabilized in 0.1% Triton X-100/PBS for 5 min (RT), washed once with PBS and blocked in blocking buffer (PBS, 1% BSA) at +4°C (overnight). Cells were stained with 1:50 Phalloidin-Alexa-555 and 1:500 anti-pTyr primary antibody (4G10) in blocking buffer for 1 hr (RT), washed 4 times with PBS, and stained with 1:500 Alexa-488 secondary anti-mouse IgG2b in blocking buffer for 1 hr (RT), washed 4 times in PBS and imaged in PBS with DeltaVision

OMX Imaging System (GE Healthcare). TIRF images of cortical actin and pTyr were processed with ImageJ macro using B220 and bright field channels to discriminate between attached WT or MIM$^{-/-}$ cells. Mean fluorescence intensities of phalloidin and pTyr staining and spreading area (determined on pTyr channel) of each cell were extracted from ~50–340 cells per experiment. Geometric means of WT and MIM$^{-/-}$ fluorescence levels and spreading area from each experiment were analyzed with paired ratio t test.

Supported lipid bilayers

Artificial planar lipid bilayers containing GPI-linked mouse ICAM-1 (200 molecules/μm^2) were formed as previously described (Grakoui et al., 1999). Briefly, unlabeled GPI-linked ICAM-1 liposomes and liposomes containing biotinylated lipids were mixed with 1,2-dioleoyl-PC (DOPC; Avanti Lipids, Inc.) at various ratios to obtain specified molecular densities. Planar membranes were assembled on FCS2 dosed chambers (Bioptechs) and blocked with PBS/2% FCS for 1 h at RT. Antigen was tethered by incubating membranes with Alexa Fluor 647-sreptavidin, followed by monobiotinylated anti-kappa light chain mAb (BD Biosciences) (20 molecules/μm^2). Alternating mixtures of CFSE-labeled and unlabeled WT and MIM$^{-/-}$ B cells at 1:1 ratio were injected into prewarmed chambers (4×10^6, +37°C) with 100 nM recombinant murine CXCL13 (PeproTech). Confocal fluorescence, differential interference contrast (DIC), and interference reflection microscopy (IRM) images were acquired in different locations at the plane of plasma membrane at 15 min after cell injection. All assays were performed in PBS, supplemented with 0.5% FCS, 0.5 g/L D-glucose, 2 mM MgCl and 0.5 mM $CaCl_2$. Images were acquired on Zeiss Axiovert LSM 510-META inverted microscope, equipped with 40x oil-immersion objective (Madrid), or Zeiss LSM 780 inverted microscope, equipped with 40x water-immersion objective (Turku), and analyzed by ImageJ and Imaris 7.0 (Bitplane). Geometric means of spreading area (determined on IRM channel), area of collected antigen and mean fluorescence intensity of antigen from each experiment (~40-500 cells per experiment) were analyzed with ration paired t test.

Ca^{2+} flux on supported lipid bilayers

Splenic WT or MIM$^{-/-}$ B cells (3.2×10^6) were resuspended in 75 μL of L-15 medium and labeled by addition of 75 μL of HBS (HEPES buffered saline, supplemented with 2.5 μM probenecid and 20 μM Fluo4 for 5 minutes at +37°C. Cells were washed in 1ml HBS-probenecid and resuspended in 500 μL HBS-probenecid for immediate injection into FCS2 chambers. Acquired movies were preprocessed with ImageJ and analyzed with CalQuo^2 software (Lee et al., 2017). Cells were categorized as single peak, oscillatory or not triggering, whereas cells showing more than two intensity peaks are classified as oscillatory.

Metabolic assay

B cells, isolated from spleens of WT and MIM$^{-/-}$ mice as described above, were seeded at a density of 10^6 cells / mL in complete RPMI. Cells were treated with IL-4 (10 ng/mL) ; anti-mouse IgM (10 µg/mL) + IL-4; LPS (4 µg/mL) or CpG (10 µg/mL) for 24 h (+37°C, 5% CO_2). Cells were then spun and resuspended in Seahorse XF RPMI, supplemented with 1 mM pyruvate, 2 mM L-glutamine and 10 mM D-glucose. Cell number was adjusted and $0.15x10^6$ cells were seeded per well on a 96-well XF plate, pre-coated with CellTak. Plate coating was done with 22.4 µg/mL CellTak in $NaHCO_3$, pH 8.0 at +4°C overnight, followed by two washings with mQ water. Seeded cells were spun at 200 g for 1 min with no break and left for 1 h at 37°C in a humidified incubator without CO_2 to attach to coated wells. Seahorse XF96 was used, following the manufacturer's instructions for XF Cell Mito Stress Test Kit. Sequentially, 1 µM oligomycin, 2 µM FCCP and 0.5 µM rotenone / antimycin A were added to the media. Oxygen consumption rate (OCR) and extracellular acidification rate (ECAR) data were recorded by WAVE software (Agilent). OCR and ECAR data were normalized to cell count and first baseline measurement of WT cells. Basal, maximum and spare respiratory capacities were extracted with area under curve analysis in GraphPad Prism.

For TMRE staining, B cells were washed in 150 µL PBS, stained with 1:500 Zombie Violet for dead cell discrimination in PBS on ice, washed 2×100µL complete RPMI and stained with 5 nM TMRE in 200 µL complete RPMI at RT for 20 min. Resuspended in 150 µL of complete RPMI, cells were immediately acquired on BD LSR Fortessa.

For Tom20 staining, B cells were stained with Zombie Violet as described above, fixed with 1.6% formaldehyde in PBS for 10 min, washed 2 × 150 µL PBS, permeabilized with 0.5% Triton X-100 in PBS for 5 min at RT, blocked for 1 h at RT. Incubation with primary Tom20 antibodies was done at 1:500 dilution for 30 min, followed by 3x 150 µL wash step and staining with 1:1000 dilution of anti-rabbit-Ax488 secondary antibodies. After 3 × 150µL wash step, cells were resuspended in 130 µL and acquired on BD LSR Fortessa. Antibody incubations, blocking and washings were done in flow cytometry buffer I on ice. Geometric mean fluorescence intensities were extracted with FlowJo software. All statistical analyses for metabolic data were done with ratio paired t test.

Figure legends

Figure 1. Normal B cell development and composition of B cell compartments in the bone marrow, spleen and peritoneal cavity of MIM-/- mice.

Flow cytometry analysis of the bone marrow, spleen and peritoneal cavity cell populations of WT and MIM-/- mice. Gating strategy is shown in Supplementary Fig. 1-1. **A.** Percentages of total $CD19^+$, $CD19^+$ IgM^+ and $CD19^-$ $CD117^+$ cells in the bone marrow. **B.** Percentages of B cell precursor and mature B cells in the bone marrow. **C.** Percentages of $CD19^+$ B cells and major T cell populations in the spleen. **D.** Percentages of major B cell subsets in the spleen. T1–3 (transitional), Fo (follicular), MZ (marginal zone) B cells. **E.** Percentages of $CD23^-CD5^+$ (B1a), $CD23^-CD5^-$ (B1b), $CD23^+CD5^-$ (Fo) B cells in the peritoneal cavity.

Figure 2. MIM deficiency leads to impaired B cell receptor signaling in response to surface-bound antigen.

A. Flow cytometry analysis of Ca^{2+} mobilization in response to B cell stimulation with soluble anti-IgM antibodies at 5 and 10 μg/mL. Data presented as ratios of Fluo-4 and Fura-red median fluorescence intensities. **B.** Immunoblot images of BCR signaling analysis in response to surface-bound anti-IgM stimulation. **C.** Quantification of phosphorylation levels of BCR signaling effector molecules shown in (B). Data presented as ratios of phosphorylated form to a total protein level and normalized to a level of WT at 3 min taken as 1. * $p<0.05$, ** $p< 0.01$, *** $p< 0.001$. Mean ± SEM.

Figure 3. $MIM^{-/-}$ B cells show diminished spreading in response to antigen immobilized on glass but normal morphology and formation of the immunological synapse in response to membrane-bound mobile ligands.

A. Scanning electron microscopy of WT and $MIM^{-/-}$ B cells at resting state and activated on the surface of anti-IgM-coated coverslips for 10 min. **B.** TIRF images of phalloidin staining at 10 min after activation on anti-IgM-coated coverslips (upper panel) and analysis of area of spreading, accumulation of pTyr and actin at the cell contact zone with coverslip (lower panel). **C.** Percentages of WT and $MIM^{-/-}$ B cells within different categories of Ca^{2+} mobilization response. **D.** IRM (upper panel), confocal fluorescence images of antigen collected by WT and $MIM^{-/-}$ B cells after 15 min activation on supported lipid bilayers containing Ax647–labeled anti-kappa antibodies (middle panel) and analysis of spreading area (based on IRM channel), antigen area and its fluorescence intensity. Scale bars, 1 μm. * $p<0.05$.

Figure 4. MIM deficiency results in impaired antigen-specific IgM and reduced levels of total IgG during T-independent immune response to NP-FICOLL.

A. Basal antibody levels of major immunoglobulin subclasses. 17-18 mice per group. **B.** Serum collection schedule and analysis of total and NP-specific antibody levels during the course of T-independent immune response. 7-8 mice per group. * $p<0.05$, ** $p< 0.01$. Mean ± SEM.

Figure 5. MIM$^{-/-}$ B cells show high metabolic activity upon stimulation with Toll-like receptor ligands, LPS and CpG.

A. Oxygen consumption rate (OCR) profiles of WT and MIM$^{-/-}$ B cells stimulated with IL-4, IgM + IL-4, LPS or CpG for 24 h and measured in Seahorse XF Cell Mito Stress Test assay. 3-4 independent experiments. Mean ± range. **B.** Analysis of baseline mitochondrial respiration, maximum and spare respiratory capacity shown in (A) Mean ± SEM. **C.** Analysis of OCR to ECAR (extracellular acidification rate) ratios at the baseline obtained in the same assay. Mean ± SEM. **D.** Analysis of mitochondrial membrane potential (TMRE) and mitochondrial mass (Tom20) in unstimulated splenic B cells. **E.** Analysis of mitochondrial membrane potential and mitochondrial mass in B cells upon 24 h culture with LPS or CpG.

References

Akkaya, M., Traba, J., Roesler, A.S., Miozzo, P., Akkaya, B., Theall, B.P., Sohn, H., Pena, M., Smelkinson, M., Kabat, J., et al. (2018). Second signals rescue B cells from activation-induced mitochondrial dysfunction and death. Nat. Immunol. *19*, 871–884.

Bolger-Munro, M., Choi, K., Scurll, J.M., Abraham, L., Chappell, R.S., Sheen, D., Dang-Lawson, M., Wu, X., Priatel, J.J., Coombs, D., et al. (2019). Arp2/3 complex-driven spatial patterning of the BCR enhances immune synapse formation, BCR signaling and cell activation. Elife *8*.

Bompard, G., Sharp, S.J., Freiss, G., and Machesky, L.M. (2005). Involvement of Rac in actin cytoskeleton rearrangements induced by MIM-B. J. Cell Sci. *118*, 5393–5403.

Boothby, M., and Rickert, R.C. (2017). Metabolic Regulation of the Immune Humoral Response. Immunity.

Bosticardo, M., Marangoni, F., Aiuti, A., Villa, A., and Grazia Roncarolo, M. (2009). Recent advances in understanding the pathophysiology of Wiskott-Aldrich syndrome. Blood *113*, 6288–6295.

Cao, M., Zhan, T., Ji, M., and Zhan, X. (2012). Dimerization is necessary for MIM-mediated membrane deformation and endocytosis. Biochem. J. *446*, 469–475.

Caro-Maldonado, A., Wang, R., Nichols, A.G., Kuraoka, M., Milasta, S., Sun, L.D., Gavin, A.L., Abel, E.D., Kelsoe, G., Green, D.R., et al. (2014). Metabolic reprogramming is required for antibody production that is suppressed in anergic but exaggerated in chronically BAFF-exposed B cells. J. Immunol. *192*, 3626–3636.

Carrasco, Y.R., and Batista, F.D. (2007). B cells acquire particulate antigen in a macrophage-rich area at the boundary between the follicle and the subcapsular sinus of the lymph node. Immunity *27*, 160–171.

Carrasco, Y.R., Fleire, S.J., Cameron, T., Dustin, M.L., and Batista, F.D. (2004). LFA-1/ICAM-1 Interaction Lowers the Threshold of B Cell Activation by Facilitating B Cell Adhesion and Synapse Formation. Immunity *20*, 589–599.

Cinamon, G., Zachariah, M.A., Lam, O.M., Foss, F.W., and Cyster, J.G. (2008). Follicular shuttling of marginal zone B cells facilitates antigen transport. Nat. Immunol. *9*, 54–62.

Coughlin, J.J., Stang, S.L., Dower, N.A., and Stone, J.C. (2005). RasGRP1 and RasGRP3 Regulate B Cell Proliferation by Facilitating B Cell Receptor-Ras Signaling. J. Immunol. *175*, 7179 LP – 7184.

Depoil, D., Fleire, S., Treanor, B.L., Weber, M., Harwood, N.E., Marchbank, K.L., Tybulewicz, V.L.J., and Batista, F.D. (2008). CD19 is essential for B cell activation by promoting B cell receptor-antigen microcluster formation in response to membrane-bound ligand. Nat. Immunol. *9*, 63–72.

van den Eertwegh, A.J., Laman, J.D., Schellekens, M.M., Boersma, W.J., and Claassen, E. (1992). Complement-mediated follicular localization of T-independent type-2 antigens: the role of marginal zone macrophages revisited. Eur. J. Immunol. *22*, 719–726.

Fahrenkamp, D., Herrmann, O., Koschmieder, S., Brümmendorf, T.H., and Schemionek, M. (2017). Mtss1(CSC156) mutant mice fail to display efficient Mtss1 protein depletion. Leukemia.

Ferguson, A.R., Youd, M.E., and Corley, R.B. (2004). Marginal zone B cells transport and deposit IgM-containing immune complexes onto follicular dendritic cells. Int. Immunol. *16*, 1411–1422.

García de Vinuesa, C., O'Leary, P., Sze, D.M., Toellner, K.M., and MacLennan, I.C. (1999). T-independent type 2 antigens induce B cell proliferation in multiple splenic sites, but exponential growth is confined to extrafollicular foci. Eur. J. Immunol.

Girkontaite, I., Missy, K., Sakk, V., Harenberg, A., Tedford, K., Pötzel, T., Pfeffer, K., and Fischer, K.-D. Lsc is required for

marginal zone B cells, regulation of lymphocyte motility and immune responses.
González-Fernández, M., Carrasco-Marín, E., Alvarez-Domínguez, C., Outschoorn, I.M., and Leyva-Cobián, F. (1997). Inhibitory effects of thymus-independent type 2 antigens on MHC class II-restricted antigen presentation: comparative analysis of carbohydrate structures and the antigen presenting cell. Cell. Immunol. *176*, 1–13.
Gonzalez-Quevedo, R., Shoffer, M., Horng, L., and Oro, A.E. (2005). Receptor tyrosine phosphatase-dependent cytoskeletal remodeling by the hedgehog-responsive gene MIM/BEG4. J. Cell Biol. *168*, 453–463.
Grakoui, A., Bromley, S.K., Sumen, C., Davis, M.M., Shaw, A.S., Allen, P.M., and Dustin, M.L. (1999). The immunological synapse: a molecular machine controlling T cell activation. Science *285*, 221–227.
Guinamard, R., Okigaki, M., Schlessinger, J., and Ravetch, J. V. (2000). Absence of marginal zone B cells in Pyk-2–deficient mice defines their role in the humoral response. Nat. Immunol. *1*, 31–36.
Haas, K.M. (2011). Programmed Cell Death 1 Suppresses B-1b Cell Expansion and Long-Lived IgG Production in Response to T Cell-Independent Type 2 Antigens. J. Immunol. *187*, 5183–5195.
Heesters, B.A., Chatterjee, P., Kim, Y.-A., Gonzalez, S.F., Kuligowski, M.P., Kirchhausen, T., and Carroll, M.C. (2013). Endocytosis and recycling of immune complexes by follicular dendritic cells enhances B cell antigen binding and activation. Immunity *38*, 1164–1175.
Jellusova, J. (2018). Cross-talk between signal transduction and metabolism in B cells. Immunol. Lett. *201*, 1–13.
Ketchum, C., Miller, H., Song, W., and Upadhyaya, A. (2014). Ligand mobility regulates B cell receptor clustering and signaling activation. Biophys. J. *106*, 26–36.
Kuokkanen, E., Šuštar, V., and Mattila, P.K. (2015). Molecular control of B cell activation and immunological synapse formation. Traffic *16*, 311–326.
Lee, A.M., Colin-York, H., and Fritzsche, M. (2017). CalQuo 2 : Automated Fourier-space, population-level quantification of global intracellular calcium responses. Sci. Rep. *7*, 1–11.
Lee, S.H., Kerff, F., Chereau, D., Ferron, F., Klug, A., and Dominguez, R. (2007). Structural basis for the actin-binding function of missing-in-metastasis. Structure *15*, 145–155.
Lin, J., Liu, J., Wang, Y., Zhu, J., Zhou, K., Smith, N., and Zhan, X. (2005). Differential regulation of cortactin and N-WASP-mediated actin polymerization by missing in metastasis (MIM) protein. Oncogene *24*, 2059–2066.
Lin, K.B.L., Freeman, S.A., Zabetian, S., Brugger, H., Weber, M., Lei, V., Dang-Lawson, M., Tse, K.W.K., Santamaria, R., Batista, F.D., et al. (2008). The rap GTPases regulate B cell morphology, immune-synapse formation, and signaling by particulate B cell receptor ligands. Immunity *28*, 75–87.
Liu, C., Miller, H., Orlowski, G., Hang, H., Upadhyaya, A., and Song, W. (2012). Actin reorganization is required for the formation of polarized B cell receptor signalosomes in response to both soluble and membrane-associated antigens. J. Immunol. *188*, 3237–3246.
Machesky, L.M., and Johnston, S.A. (2007). MIM: a multifunctional scaffold protein. J. Mol. Med. (Berl). *85*, 569–576.
Mattila, P.K., Salminen, M., Yamashiro, T., and Lappalainen, P. (2003). Mouse MIM, a tissue-specific regulator of cytoskeletal dynamics, interacts with ATP-actin monomers through its C-terminal WH2 domain. J. Biol. Chem. *278*, 8452–8459.
Mattila, P.K., Pykäläinen, A., Saarikangas, J., Paavilainen, V.O., Vihinen, H., Jokitalo, E., and Lappalainen, P. (2007). Missing-in-metastasis and IRSp53 deform PI(4,5)P2-rich membranes by an inverse BAR domain-like mechanism. J. Cell Biol. *176*, 953–964.
Mattila, P.K., Feest, C., Depoil, D., Treanor, B., Montaner, B., Otipoby, K.L., Carter, R., Justement, L.B., Bruckbauer, A., and Batista, F.D. (2013). The actin and tetraspanin networks organize receptor nanoclusters to regulate B cell receptor-

mediated signaling. Immunity *38*, 461–474.
Mattila, P.K., Batista, F.D., and Treanor, B. (2016). Dynamics of the actin cytoskeleton mediates receptor cross talk: An emerging concept in tuning receptor signaling. J. Cell Biol. *212*.
McLeod, S.J., Shum, A.J., Lee, R.L., Takei, F., and Gold, M.R. (2004). The Rap GTPases Regulate Integrin-mediated Adhesion, Cell Spreading, Actin Polymerization, and Pyk2 Tyrosine Phosphorylation in B Lymphocytes. J. Biol. Chem. *279*, 12009–12019.
Mérida, I., Carrasco, S., and Avila-Flores, A. (2010). Diacylglycerol Signaling: The C1 Domain, Generation of DAG, and Termination of Signals. In Protein Kinase C in Cancer Signaling and Therapy, (Totowa, NJ: Humana Press), pp. 55–78.
Mongini, P.K., Stein, K.E., and Paul, W.E. (1981). T cell regulation of IgG subclass antibody production in response to T-independent antigens. J. Exp. Med. *153*, 1–12.
Mongini, P.K., Longo, D.L., and Paul, W.E. (1984). T cell regulation of immunoglobulin class expression in the B cell response to TNP-Ficoll: characterization of the T cell responsible for preferential enhancement of the IgG2a response. J. Immunol. *132*, 1647–1653.
Nolte, M.A., Beliën, J.A.M., Schadee-Eestermans, I., Jansen, W., Unger, W.W.J., van Rooijen, N., Kraal, G., and Mebius, R.E. (2003). A Conduit System Distributes Chemokines and Small Blood-borne Molecules through the Splenic White Pulp. J. Exp. Med. *198*, 505–512.
O'Neill, L.A.J., Kishton, R.J., and Rathmell, J. (2016). A guide to immunometabolism for immunologists. Nat. Rev. Immunol. *16*, 553.
Otero, D.C., Omori, S.A., and Rickert, R.C. (2001). CD19-dependent activation of Akt kinase in B-lymphocytes. J. Biol. Chem.
Perlmutter, R.M., Hansburg, D., Briles, D.E., Nicolotti, R.A., Davie, J.M., and Smale, S.T. (1978). Subclass restriction of murine anti-carbohydrate antibodies. J. Immunol.
Petrov, P., Sarapulov, A. V, Eöry, L., Scielzo, C., Scarfò, L., Smith, J., Burt, D.W., and Mattila, P.K. (2019). Computational analysis of the evolutionarily conserved Missing In Metastasis/Metastasis Suppressor 1 gene predicts novel interactions, regulatory regions and transcriptional control. Sci. Rep. *9*, 4155.
Price, M.J., Patterson, D.G., Scharer, C.D., and Boss, J.M. (2018). Progressive Upregulation of Oxidative Metabolism Facilitates Plasmablast Differentiation to a T-Independent Antigen. Cell Rep. *23*, 3152–3159.
Rickert, R.C., Rajewsky, K., and Roes, J. (1995). Impairment of T-cell-dependent B-cell responses and B-1 cell development in CD19-deficient mice. Nature *376*, 352–355.
Saarikangas, J., Mattila, P.K., Varjosalo, M., Bovellan, M., Hakanen, J., Calzada-Wack, J., Tost, M., Jennen, L., Rathkolb, B., Hans, W., et al. (2011). Missing-in-metastasis MIM/MTSS1 promotes actin assembly at intercellular junctions and is required for integrity of kidney epithelia. J. Cell Sci. *124*, 1245–1255.
Scher, I. (1982). CBA/N immune defective mice; evidence for the failure of a B cell subpopulation to be expressed. Immunol. Rev. *64*, 117–136.
Schnyder, T., Castello, A., Feest, C., Harwood, N.E., Oellerich, T., Urlaub, H., Engelke, M., Wienands, J., Bruckbauer, A., and Batista, F.D. (2011). B Cell Receptor-Mediated Antigen Gathering Requires Ubiquitin Ligase Cbl and Adaptors Grb2 and Dok-3 to Recruit Dynein to the Signaling Microcluster. Immunity *34*, 905–918.
Shaheen, S., Wan, Z., Li, Z., Chau, A., Li, X., Zhang, S., Liu, Y., Yi, J., Zeng, Y., Wang, J., et al. (2017). Substrate stiffness governs the initiation of B cell activation by the concerted signaling of PKCβ and focal adhesion kinase. Elife *6*.
El Shikh, M.E.M., El Sayed, R.M., Sukumar, S., Szakal, A.K., and Tew, J.G. (2010). Activation of B cells by antigens on follicular dendritic cells. Trends Immunol.

Slack, J., Der-Balian, G.P., Nahm, M., and Davie, J.M. (1980). Subclass restriction of murine antibodies. II. The IgG plaque-forming cell response to thymus-independent type 1 and type 2 antigens in normal mice and mice expressing an X-linked immunodeficiency. J. Exp. Med. *151*, 853–862.

Snapper, C.M. (2018). Distinct immunologic properties of soluble versus particulate antigens. Front. Immunol. *9*.

Spillane, K.M., and Tolar, P. (2017). B cell antigen extraction is regulated by physical properties of antigen-presenting cells. J. Cell Biol. *216*, 217–230.

Su, T.T., Guo, B., Kawakami, Y., Sommer, K., Chae, K., Humphries, L.A., Kato, R.M., Kang, S., Patrone, L., Wall, R., et al. (2002). PKC-β controls IκB kinase lipid raft recruitment and activation in response to BCR signaling. Nat. Immunol. *3*, 780–786.

Tolar, P. (2017). Cytoskeletal control of B cell responses to antigens. Nat. Rev. Immunol. *17*, 621–634.

Tolar, P., and Spillane, K.M. (2014). Force generation in B-cell synapses: mechanisms coupling B-cell receptor binding to antigen internalization and affinity discrimination. Adv. Immunol. *123*, 69–100.

Treanor, B., Depoil, D., Gonzalez-Granja, A., Barral, P., Weber, M., Dushek, O., Bruckbauer, A., and Batista, F.D. (2010). The membrane skeleton controls diffusion dynamics and signaling through the B cell receptor. Immunity *32*, 187–199.

Wan, Z., Zhang, S., Fan, Y., Liu, K., Du, F., Davey, A.M., Zhang, H., Han, W., Xiong, C., and Liu, W. (2013). B Cell Activation Is Regulated by the Stiffness Properties of the Substrate Presenting the Antigens. J. Immunol. *190*.

Wan, Z., Chen, X., Chen, H., Ji, Q., Chen, Y., Wang, J., Cao, Y., Wang, F., Lou, J., Tang, Z., et al. (2015). The activation of IgM- or isotype-switched IgG- and IgE-BCR exhibits distinct mechanical force sensitivity and threshold. Elife *4*.

Wan, Z., Xu, C., Chen, X., Xie, H., Li, Z., Wang, J., Ji, X., Chen, H., Ji, Q., Shaheen, S., et al. (2018). PI(4,5)P2 determines the threshold of mechanical force–induced B cell activation. J. Cell Biol. *217*, 2565 LP – 2582.

Woodings, J.A., Sharp, S.J., and Machesky, L.M. (2003). MIM-B, a putative metastasis suppressor protein, binds to actin and to protein tyrosine phosphatase delta. Biochem. J. *371*, 463–471.

Yamagishi, A., Masuda, M., Ohki, T., Onishi, H., and Mochizuki, N. (2004). A novel actin bundling/filopodium-forming domain conserved in insulin receptor tyrosine kinase substrate p53 and missing in metastasis protein. J. Biol. Chem. *279*, 14929–14936.

Young, R.M., and Staudt, L.M. (2013). Targeting pathological B cell receptor signalling in lymphoid malignancies. Nat. Rev. Drug Discov. *12*, 229–243.

Yu, D., Zhan, X.H., Niu, S., Mikhailenko, I., Strickland, D.K., Zhu, J., Cao, M., and Zhan, X. (2011). Murine missing in metastasis (MIM) mediates cell polarity and regulates the motility response to growth factors. PLoS One *6*, e20845.

Yu, D., Zhan, X.H., Zhao, X.F., Williams, M.S., Carey, G.B., Smith, E., Scott, D., Zhu, J., Guo, Y., Cherukuri, S., et al. (2012). Mice deficient in MIM expression are predisposed to lymphomagenesis. Oncogene *31*, 3561–3568.

Zeng, Y., Yi, J., Wan, Z., Liu, K., Song, P., Chau, A., Wang, F., Chang, Z., Han, W., Zheng, W., et al. (2015). Substrate stiffness regulates B-cell activation, proliferation, class switch, and T-cell-independent antibody responses in vivo. Eur. J. Immunol. *45*, 1621–1634.

Zhan, T., Cao, C., Li, L., Gu, N., Civin, C.I., and Zhan, X. (2016). MIM regulates the trafficking of bone marrow cells via modulating surface expression of CXCR4. Leukemia *30*, 1327–1334.

Figure 1

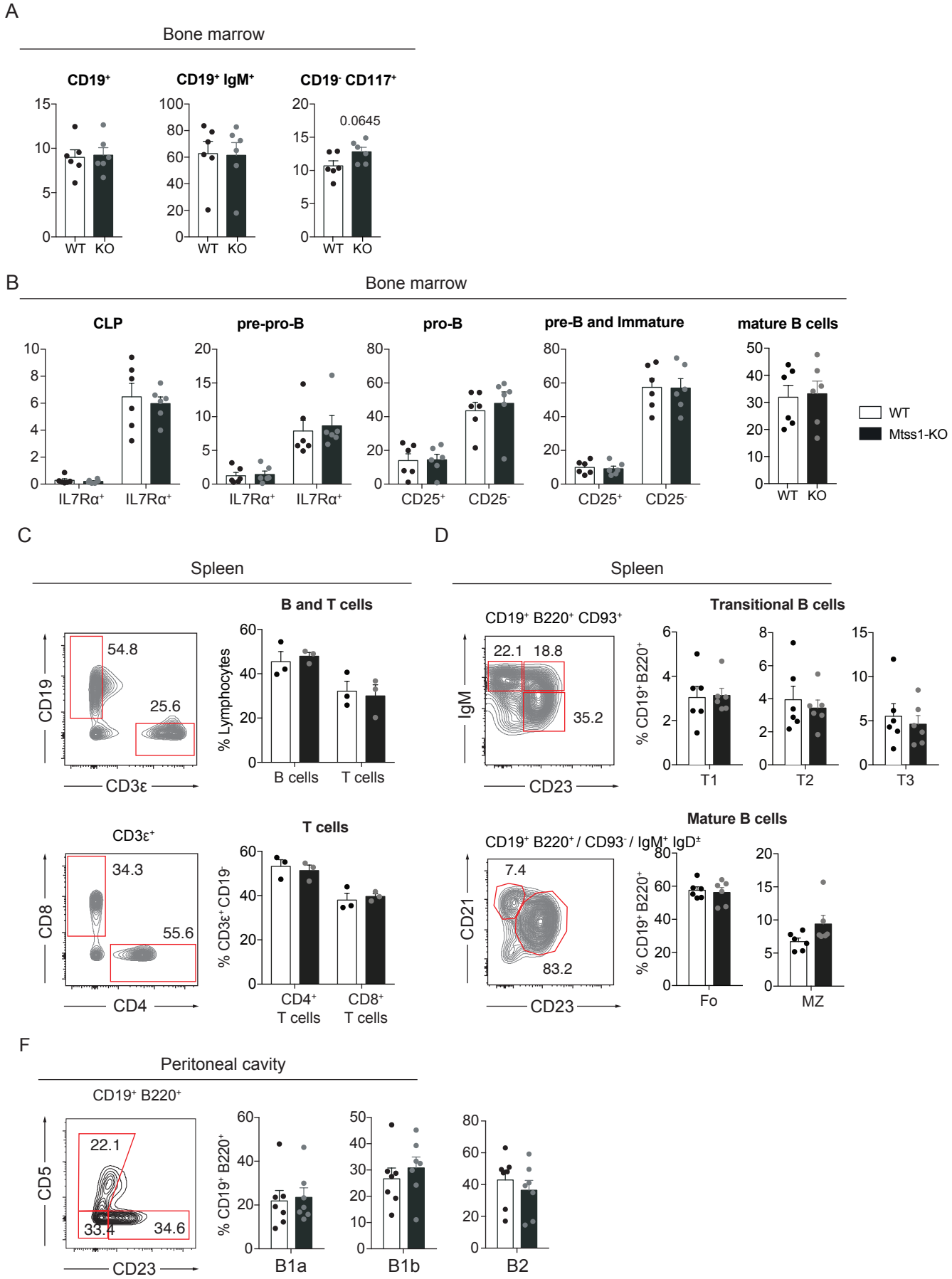
A
Bone marrow
CD19+
CD19+ IgM+
CD19- CD117+
0.0645
WT KO
B
Bone marrow
CLP
pre-pro-B
pro-B
pre-B and Immature
mature B cells
IL7Rα+
CD25+
CD25-
WT
Mtss1-KO
C
Spleen
B and T cells
54.8
25.6
CD19
CD3ε
% Lymphocytes
B cells
T cells
CD3ε+
34.3
55.6
CD8
CD4
T cells
% CD3ε+ CD19-
CD4+ T cells
CD8+ T cells
D
Spleen
CD19+ B220+ CD93+
22.1
18.8
35.2
IgM
CD23
Transitional B cells
% CD19+ B220+
T1
T2
T3
Mature B cells
CD19+ B220+ / CD93- / IgM+ IgD±
7.4
83.2
CD21
Fo
MZ
F
Peritoneal cavity
CD19+ B220+
22.1
33.4
34.6
CD5
CD23
% CD19+ B220+
B1a
B1b
B2

Figure 2

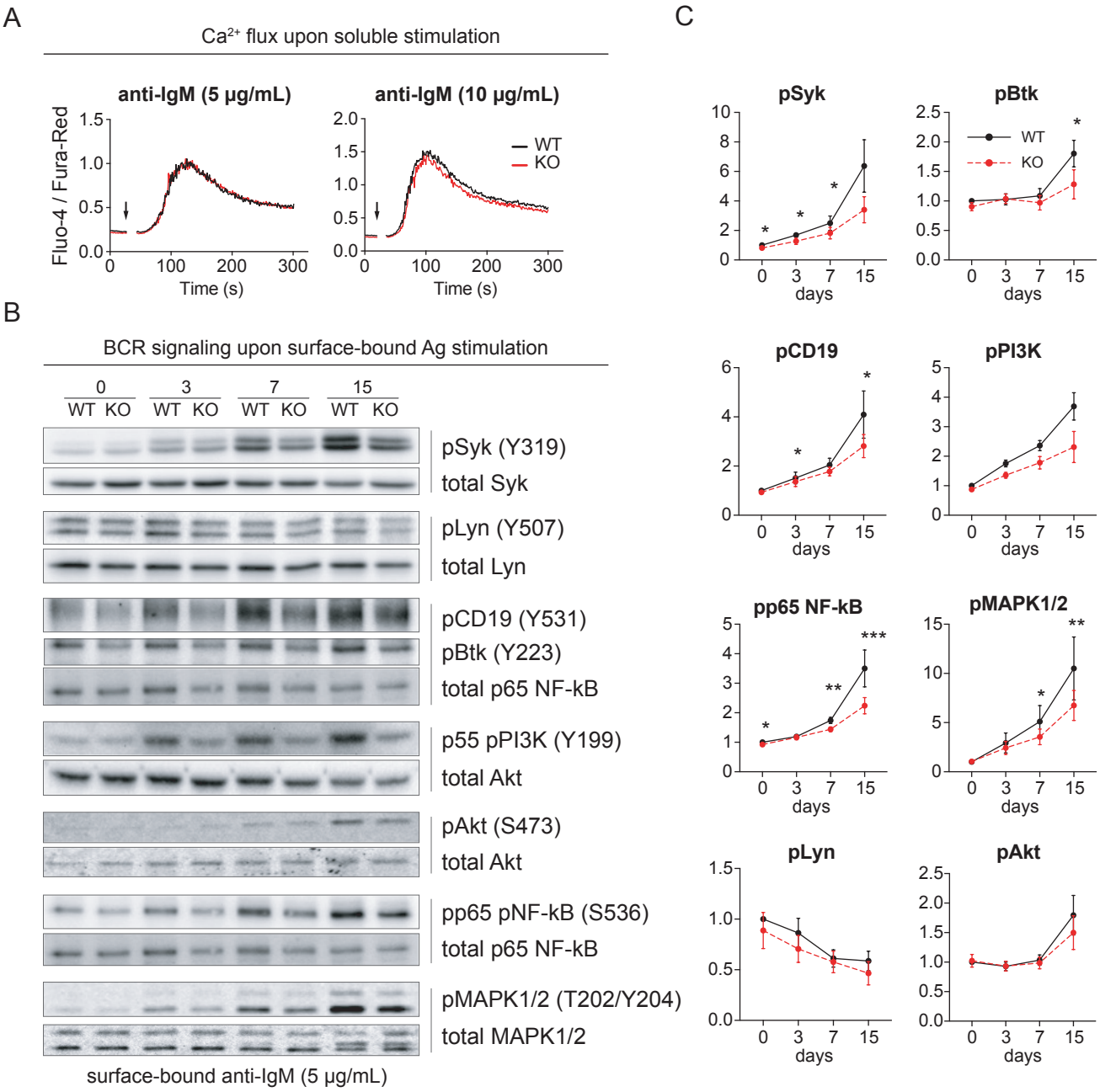
A
Ca2+ flux upon soluble stimulation
anti-IgM (5 µg/mL)
anti-IgM (10 µg/mL)
Fluo-4 / Fura-Red
Time (s)
WT
KO
B
BCR signaling upon surface-bound Ag stimulation
0
3
7
15
WT KO
pSyk (Y319)
total Syk
pLyn (Y507)
total Lyn
pCD19 (Y531)
pBtk (Y223)
total p65 NF-kB
p55 pPI3K (Y199)
total Akt
pAkt (S473)
total Akt
pp65 pNF-kB (S536)
total p65 NF-kB
pMAPK1/2 (T202/Y204)
total MAPK1/2
surface-bound anti-IgM (5 µg/mL)
C
pSyk
pBtk
pCD19
pPI3K
pp65 NF-kB
pMAPK1/2
pLyn
pAkt
days

Figure 3

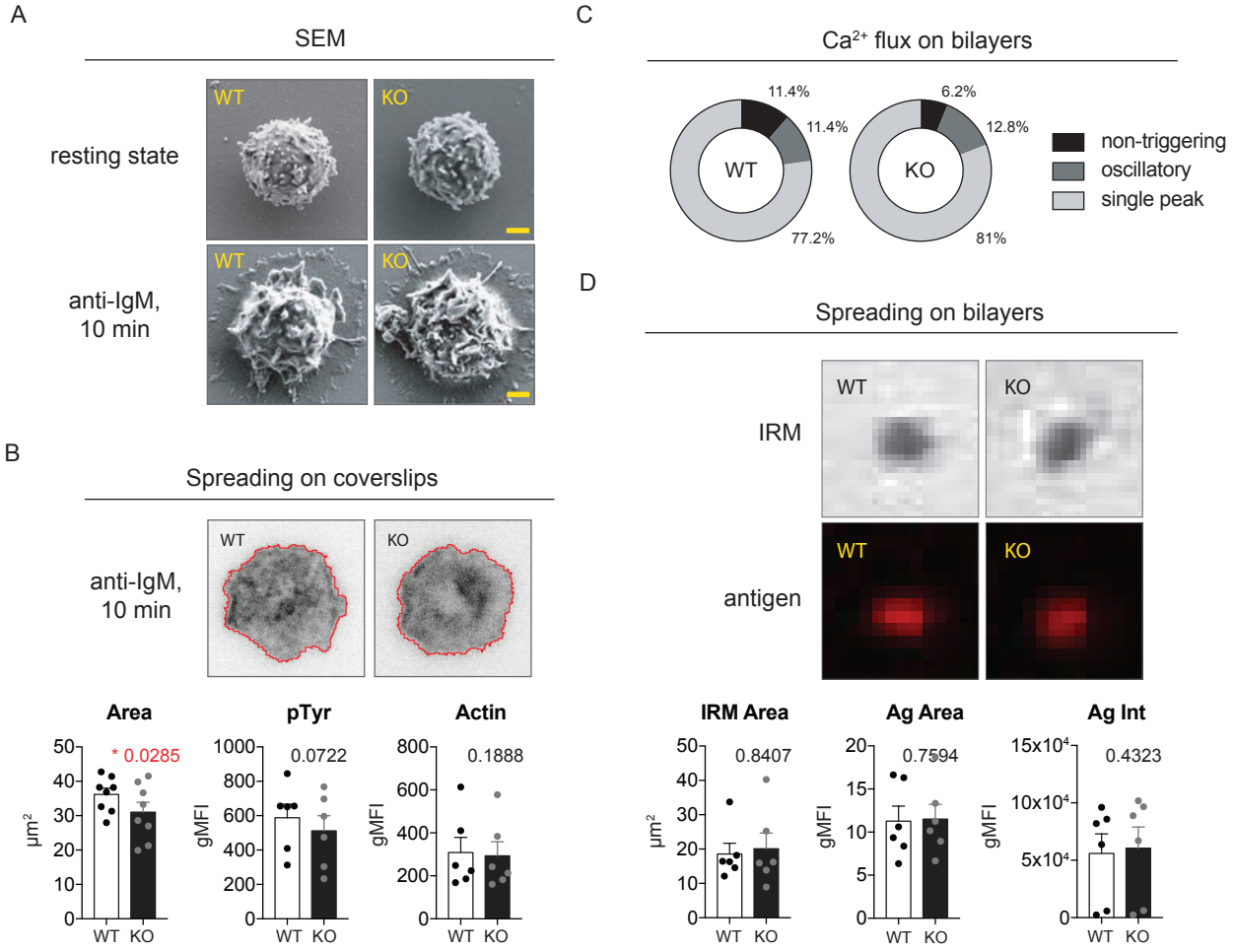
A
SEM
resting state
anti-IgM, 10 min
WT
KO
B
Spreading on coverslips
anti-IgM, 10 min
Area
pTyr
Actin
* 0.0285
0.0722
0.1888
μm²
gMFI
C
Ca²⁺ flux on bilayers
11.4%
11.4%
77.2%
6.2%
12.8%
81%
non-triggering
oscillatory
single peak
D
Spreading on bilayers
IRM
antigen
IRM Area
Ag Area
Ag Int
0.8407
0.7594
0.4323

Figure 4

A

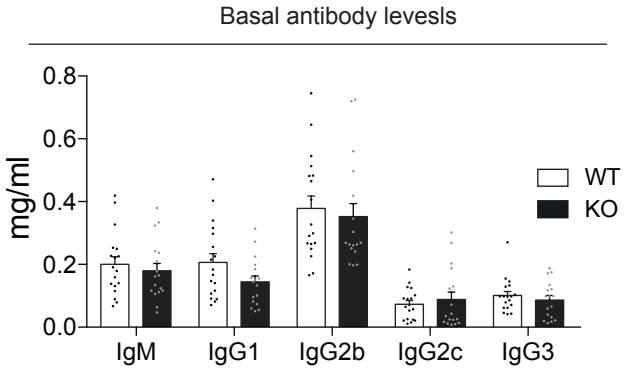
Basal antibody levesls
mg/ml
0.8
0.6
0.4
0.2
0.0
WT
KO
IgM
IgG1
IgG2b
IgG2c
IgG3

B

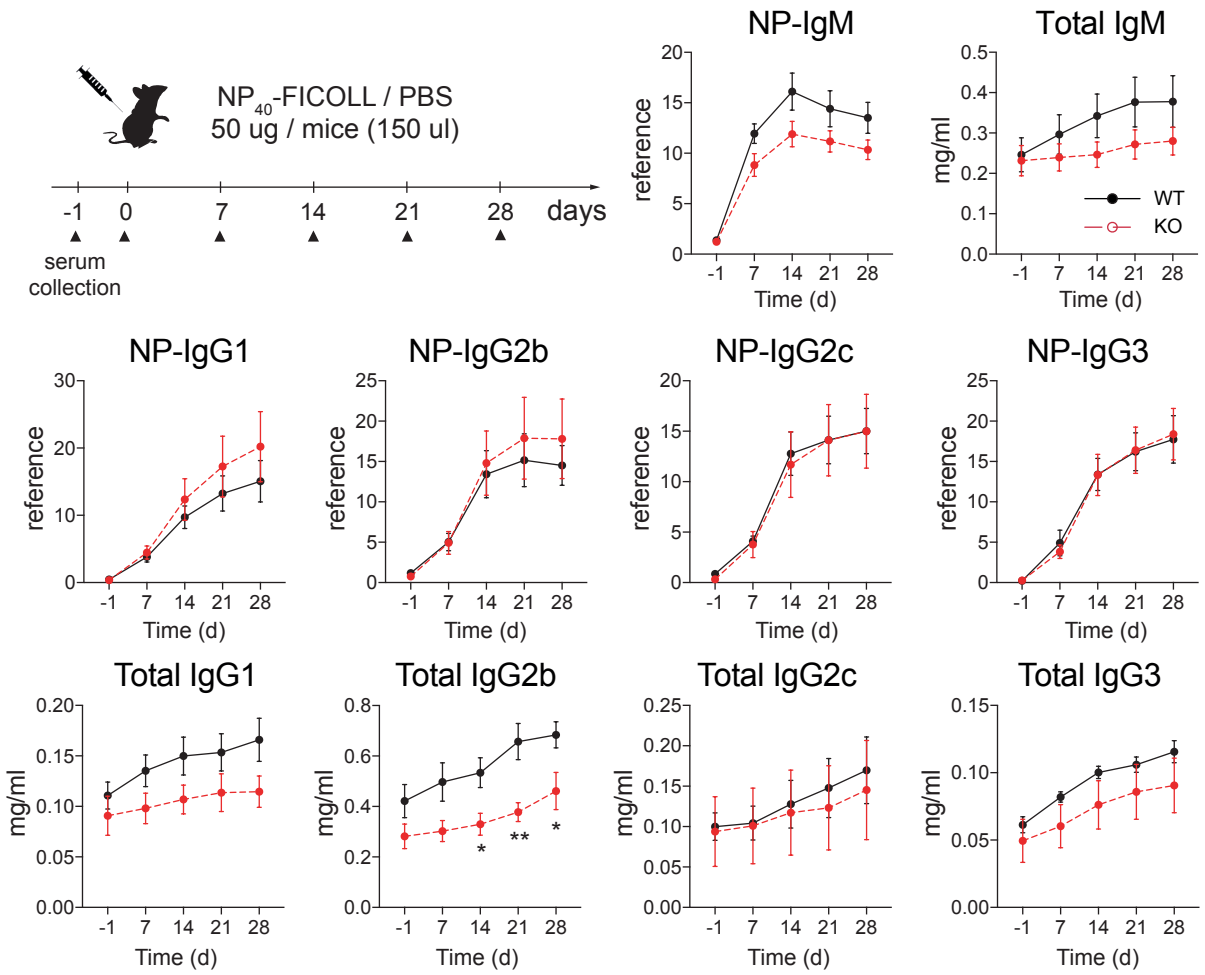
NP40-FICOLL / PBS
50 ug / mice (150 ul)
-1
0
7
14
21
28
days
serum collection
NP-IgM
Total IgM
NP-IgG1
NP-IgG2b
NP-IgG2c
NP-IgG3
Total IgG1
Total IgG2b
Total IgG2c
Total IgG3
reference
mg/ml
Time (d)
WT
KO
*
**
*

Figure 5

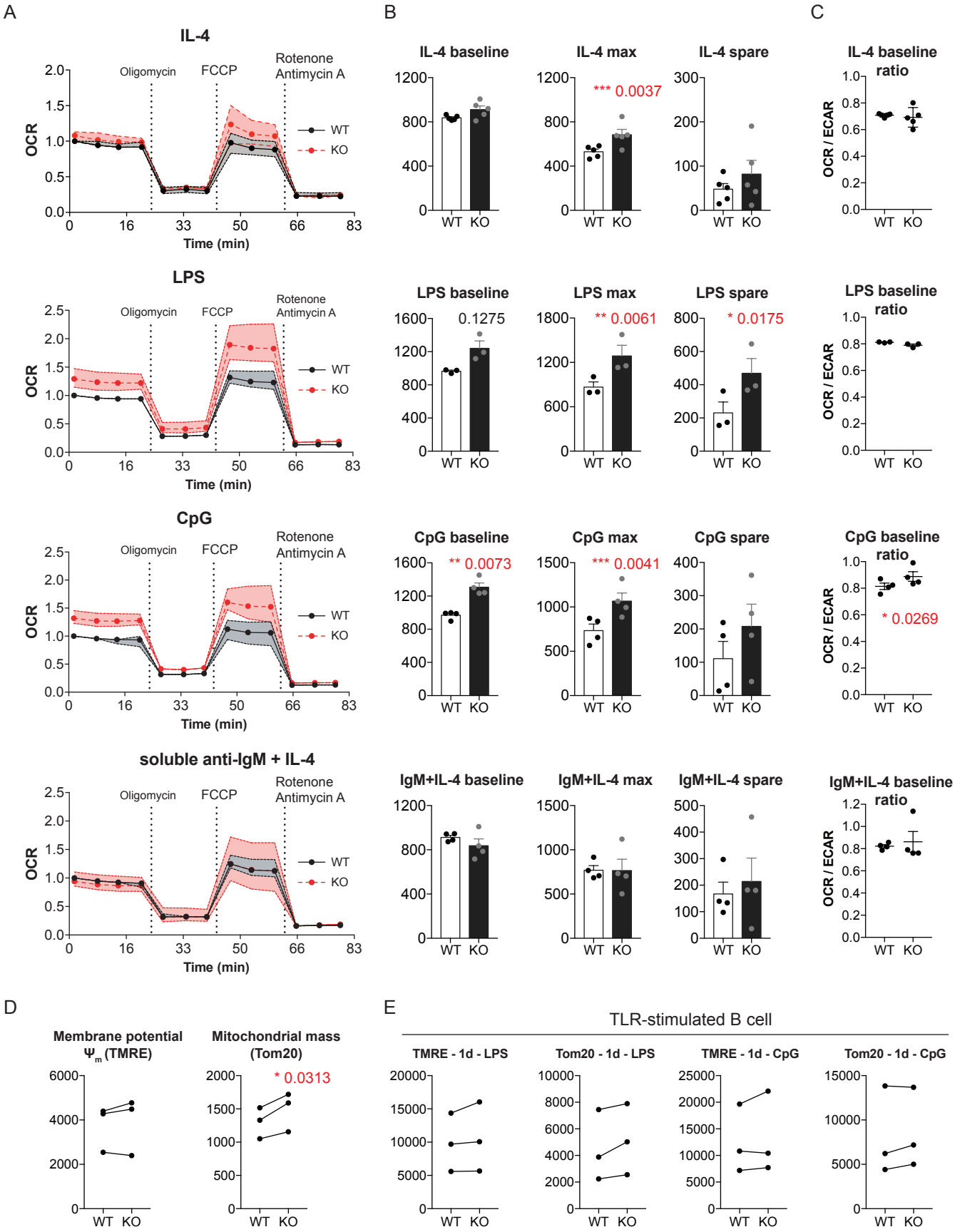
A
IL-4
Oligomycin
FCCP
Rotenone
Antimycin A
OCR
Time (min)
WT
KO
LPS
CpG
soluble anti-IgM + IL-4
B
IL-4 baseline
IL-4 max
*** 0.0037
IL-4 spare
LPS baseline
0.1275
LPS max
** 0.0061
LPS spare
* 0.0175
CpG baseline
** 0.0073
CpG max
*** 0.0041
CpG spare
IgM+IL-4 baseline
IgM+IL-4 max
IgM+IL-4 spare
C
IL-4 baseline ratio
LPS baseline ratio
CpG baseline ratio
* 0.0269
IgM+IL-4 baseline ratio
OCR / ECAR
D
Membrane potential
Ψ_m (TMRE)
Mitochondrial mass
(Tom20)
* 0.0313
E
TLR-stimulated B cell
TMRE - 1d - LPS
Tom20 - 1d - LPS
TMRE - 1d - CpG
Tom20 - 1d - CpG